> TSTE-00006-2024 <

Interaction Modeling and Stability Analysis of Grid-forming Energy Storage System Based on SISO Transfer Functions

Kezan Zhang, Mengxuan Shi, Xia Chen, *Senior Member*, *IEEE*, Dejun Shao, Youping Xu, and Yin Chen

***Abstract*—With the rapid expansion of photovoltaic (PV), grid-forming energy storage systems (GFM-ESS) have been widely employed for inertia response and voltage support to enhance the dynamic characteristics. Converters with different synchronization methods represent significant differences in dynamic behavior. The interactions between grid-forming (GFM) and grid-following (GFL) devices with multi-time scale control may lead to small-signal instability in hybrid systems. This paper investigates a grid-connected system comprising a grid-forming energy storage system and a grid-following PV system (GFL-PV). Based on single-input-single-output (SISO) transfer functions, a dynamic interaction model for the PV-ESS system is established. Combining the open-loop transfer functions of full-loop and sub-loop, the proposed model reveals how GFM-ESS modifies the dynamic characteristics of GFL-PV under weak grid conditions. Subsequently, the impact of different control loops and parameters on the small-signal stability of the system is analyzed. The stability margins of both devices are also compared through the SISO model. Electromagnetic transient simulation results in MATLAB/Simulink and experiments validate the effectiveness of the proposed models and analyses.**

***Index Terms*—Single input single output, photovoltaic system, grid-forming; energy storage systems, interaction modeling;**

I. Introduction

Power electronic devices are being extensively integrated into power systems with the development of renewable energy sources (RESs), high-voltage DC transmission, and other technologies, profoundly altering the dynamic characteristics of modern power systems [1]-[2]. Among these changes, the issues of grid weakening and reduced inertia are particularly prominent [3]-[5]. In response to the issues, energy storage systems (ESS) have been widely employed for applications such as inertial response, frequency regulation, and voltage control. ESS operated in the PQ (active-reactive) control mode can achieve grid regulation effects by enhancing the power outer loop. However, ESS synchronized via Phase-Locked Loop (PLL) lacks active support capabilities and cannot control the grid frequency and voltage autonomously. With the increasing penetration of renewable energy sources, they are no longer sufficient to provide the system stability required by the grid [6]-[9].

Considering the issues of grid-following (GFL) control in RESs dominated grid, a viable approach to providing the necessary stability for the power system is to configure ESS in grid-forming (GFM) mode [10]-[11]. GFM-ESS can exhibit voltage source characteristics similar to synchronous generators to actively support the grid and enhance grid strength [12]. In addition, GFM-ESS based on virtual synchronous control can provide a range of services to the grid, including virtual inertia and fault ride-through capability.

Due to different synchronization modes, there are significant differences in the dynamic behaviors of GFM and GFL converters: GFL converters synchronized based on PLL exhibit reduced stability margins as the grid short-circuit ratio (SCR) decreases, leading to instability issues in weak grids [13]-[14]. However, as the grid strength decreases, GFM converters synchronized based on power synchronization exhibit reduced interactions with the AC grid, displaying better stability [15]-[16]. It's pointed out in [17]-[18] that GFM converters are similarly exposed to the risk of synchronous and subsynchronous oscillations in a strong grid. Therefore, devices with different synchronization methods have varying applicability to grid strength. The synchronization stability issues in hybrid systems composed of grid-following and grid-forming devices require further research.

Most of the existing research on modeling hybrid systems containing both GFL and GFM converters relies on impedance-based or state-space methods [19]-[21]. Reference [22] conducted stability and interaction studies on the interconnected system using the impedance model, indicating that the inclusion of GFM converters in weak grids can enhance the stability of GFL converters. However, strong grids with GFM converters and low network impedance may experience low-frequency oscillations. In [23], a generalized impedance model was proposed for multiple GFL and GFM converters. It's proved that the determinant of total admittance can be directly used for stability demonstration in MIMO AC systems. A three-step procedure is suggested for stability assessment. A state-

This work was supported by the 2023 Science and Technology Project of Central-China Branch of State Grid Corporation of China Limited (The Research on the Impact and Countermeasures of Security and Stability of the Central China Power Grid under the Situation of Large-Scale New Energy Base Concentrated Access) under Grant 521400230006. Paper no. TSTE-00006-2024. (*Corresponding author: Yin Chen.*)

K. Zhang, X. Chen are with the College of Electrical and Electronic En gineering, Huazhong University of Science and Technology, Wuhan 43007 0, China (email: zhangkezan@hust.edu.cn; cxhust@hust.edu.cn)

Y. Chen is with the Department of Electronic and Electrical Engineering, University of Strathclyde, Glasgow G1 1XW, U.K. (e-mail: yin.chen.101@strath.ac.uk.)

M. Shi, D. Shao, and Y. Xu are with the CentralChina Branch of State Grid Corporation of China, Wuhan 430077, China (email: shimengxuan31 7@126.com, shaodjun@163.com, xyp13507159051@163.com)

space model was established in [24] for multiple parallel-connected DFIGs and virtual synchronous generators (VSGs), employing characteristic root locus to determine system-similar modes. It was noted that the voltage control loop of VSG and the current control loop of DFIG in hybrid systems could experience open-loop mode resonance. This interaction was mitigated by introducing additional damping controllers, which improved the small-signal stability of the system. Reference [25] used both impedance and state-space methods to model offshore wind power plants and GFM-ESS. Transfer function and pole-zero analyses were employed to evaluate the coupling effects on closed-loop control bandwidth and power control loops. Sensitivity analysis was conducted to determine critical controller parameter tuning methods under different conditions. The models established for hybrid systems in the above references are high-order, strongly coupled Multiple-Input Multiple-Output (MIMO) models. The entire system is modeled without internal divisions, which makes it challenging to clarify the actual physical meaning and provide stability margins. In [26], a SISO model was proposed for analyzing the grid-synchronization stability of a PLL-based power converter, providing a different perspective on modeling. However, the hybrid GFL-GFM systems have not been considered. The interaction characteristics between the two converters remain unclear.

In order to explore the influence of interactions within the hybrid system on small-signal stability, this paper proposes a SISO interactive analysis model containing a grid-following photovoltaic (GFL-PV) station and a GFM-ESS. The analyses of the proposed model reveal the interaction mechanism between the two devices. Furthermore, the stability margins of the two converters can be individually quantified based on different transfer functions. The simulation and OPAL-RT experiment are combined to validate the model's effectiveness and analyses. The main contributions are as follows.

1) The SISO interaction model of the PV-ESS system is proposed, addressing the challenges of analyzing MIMO systems. The proposed model focuses on the output phase of each device and can completely reflect the unstable problems caused by different control loops. Every derived transfer function possesses clear physical meaning.
2) Through the proposed model, the supportive effects of GFM-ESS with different control parameters are evaluated, along with how GFL-PV influences the stability of GFM-ESS. The effects of converters can be decomposed into the superposition of active and passive components, providing a better explanation of the interaction mechanism. The conclusions drawn bear significant implications for the design of system controller parameters.
3) The stability margins of each device can be individually determined from its dominant loop, which cannot be achieved in other small-signal models [25]. Specifically, the stability of the system can be determined by two open-loop transfer functions, corresponding to the dominant loops governed by GFM and GFL. This helps identify the weaker device in the system and improves its stability.

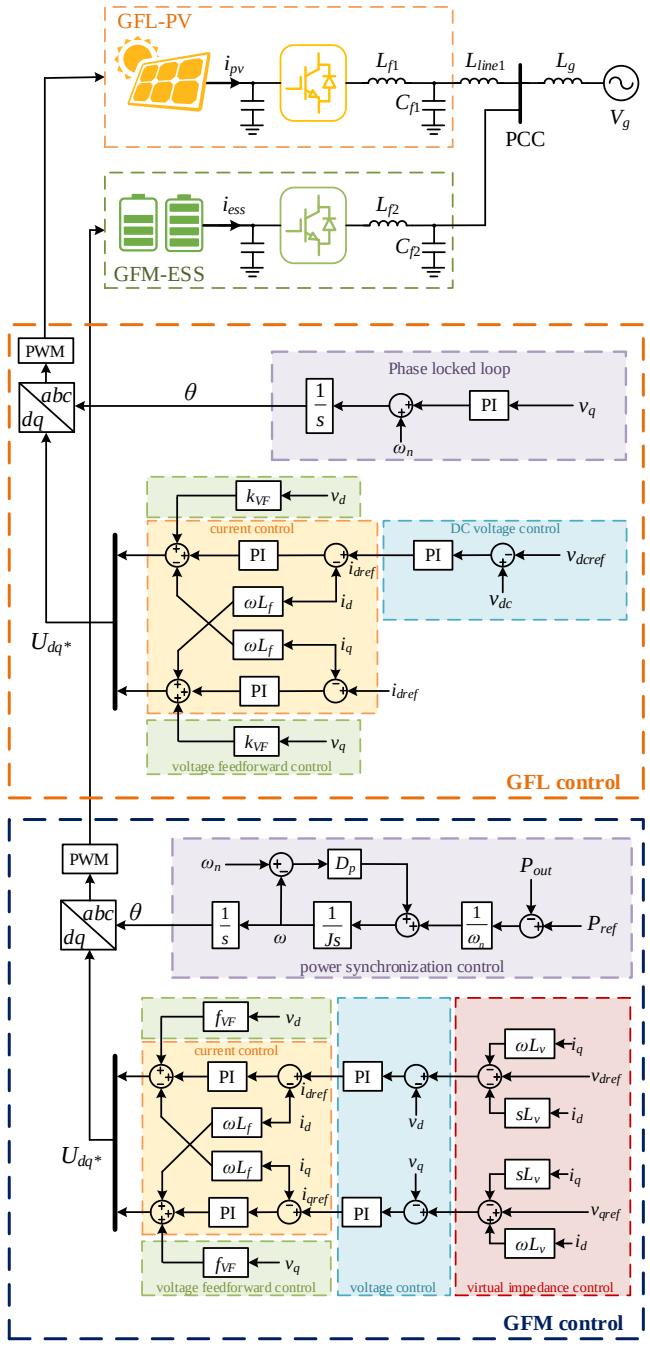

Fig. 1 Diagram of a simplified PV system with GFM-ESS.

The rest of this paper is organized as follows: Section II establishes the complex vector form of the impedance models for GFL-PV and GFM-ESS. Subsequently, a SISO interactive analysis model for the PV-ESS system is derived. Based on the proposed model, Section III investigates the interaction patterns between the converters with different control parameters through a stability analysis. The time-domain simulation results and experiment validation are presented in Section IV. Section V concludes the paper.

II. The Small-Signal Model of PV-ESS System

The simplified topology of a PV system equipped with a

GFM-ESS is illustrated in Fig. 1. The PV array, filtered by an LC filter, is grid-connected through a three-phase power converter, while the GFM-ESS is similarly connected in parallel to the point of common coupling (PCC) through a similar pathway. The external grid is represented by an equivalent circuit with an inductor in series, symbolizing an infinite voltage source. The control structure of the two converters is also depicted in Fig. 1. The reference voltage of the bridge arms is modulated through PWM to generate the drive signals for the switching devices.

The inner control loops of the converters will be considered first and combined with the outer loop dynamics to obtain the proposed SISO model. Since the inner loop impedance of the converters typically satisfies symmetrical conditions, for the sake of brevity, we adopt a complex vector form of the impedance model in Section II. B. Firstly, the general form of the impedance model and how to transform it into a complex vector form will be introduced in Section II. A.

A. Complex Vector Form of the Impedance Model

In the *dq* coordinate system, impedance models are commonly described by a 2×2 matrix. The transfer function matrix $\mathbf{Z}_{dq}^{m}$ consists of four elements: Z_{dd} and Z_{qq} represent the self-impedances along the *dq* axes, while Z_{dq} and Z_{qd} denote the mutual impedances, reflecting the coupling between the two coordinate axes. Considering a left multiplication of the voltage and current vectors by the matrix **T**, the impedance matrix can be transformed into a complex vector form, as shown in (2).

$$\begin{bmatrix} v_d \\ v_q \end{bmatrix} = \underbrace{\begin{bmatrix} Z_{dd} & Z_{dq} \\ Z_{qd} & Z_{qq} \end{bmatrix}}_{\mathbf{Z}_{dq}^{m}} \begin{bmatrix} i_d \\ i_q \end{bmatrix} \tag{1}$$

$$\mathbf{v}_{dq\pm} = \mathbf{Z}_{dq\pm}^{m}\mathbf{i}_{dq\pm}$$

$$\begin{cases} \mathbf{v}_{dq\pm} = \mathbf{T}\mathbf{v}_{dq} \\ \mathbf{i}_{dq\pm} = \mathbf{T}\mathbf{i}_{dq} \\ \mathbf{Z}_{dq\pm}^{m} = \mathbf{T}\mathbf{Z}_{dq}^{m}\mathbf{T}^{-1} \end{cases} \quad \mathbf{T} = \begin{bmatrix} 1 & j \\ 1 & -j \end{bmatrix} \tag{2}$$

In complex vector form, the voltage and current are transformed from original *dq* components into two conjugate complex vectors: $v_{dq+} = v_d + jv_q$ and $v_{dq-} = v_d - jv_q$. The impedance matrix is also transformed from its original four components into two pairs of independent conjugate components [27], as described in (3).

$$\mathbf{Z}_{dq\pm}^{m} = \begin{bmatrix} Z_{dq+} & Z_{dq-} \\ \bar{Z}_{dq-} & \bar{Z}_{dq+} \end{bmatrix}$$

$$\begin{cases} Z_{dq+} = \dfrac{Z_{dd} + Z_{qq}}{2} + j\dfrac{Z_{qd} - Z_{dq}}{2} \\ Z_{dq-} = \dfrac{Z_{dd} - Z_{qq}}{2} + j\dfrac{Z_{qd} + Z_{dq}}{2} \end{cases} \tag{3}$$

Notice that if the impedance matrix $\boldsymbol{Z}_{dq}^{m}$ satisfies the symmetric condition, namely: $Z_{dd} = Z_{qq}$ and $Z_{dq} = -Z_{qd}$, then the Z_{dq-} component in (3) equals to zero, and the impedance matrix $\boldsymbol{Z}_{dq\pm}^{m}$ in complex vector form becomes a diagonal matrix. It can be observed in the following sections that due to the symmetric condition being satisfied by both the grid impedance and the inner loop impedance of the converter, the impedance matrix in complex vector form significantly simplifies the derivation process.

B. Admittance Model of Inner Loop

The small-signal admittance models for the GFL-PV and GFM-ESS in the local coordinate system are established in this subsection. The control strategy for GFL-PV is delineated in Fig. 1: the deployment of the Synchronous Reference Frame Phase-Locked Loop (SRF-PLL) ensures grid synchronization, with the current loop command originating from the preceding DC voltage control. Notably, the reactive power control loop is omitted, and the converter's dynamic performance is augmented through the application of voltage feedforward (VFF) control. Since the dynamics of the DC side are slow enough to have minimal impact on the small-signal stability of the GFL converter. The complex vector form of the inner loop admittance model can be simplified, and the detailed derivation is provided in Appendix A.

$$\begin{cases} Y_{IV1+} = \dfrac{1-k_{VF}}{-PI_{CCL}(s) - sL_{f1}} - sC_{f1} - j\omega C_{f1} \\ Y_{IV1-} = 0 \end{cases} \tag{4}$$

where L_{f1}, C_{f1} denotes the parameters of the *LC* filter, $PI_{CCL}(s)$ represents the transfer function of the PI controller for the current loop and k_{VF} is the voltage feedforward coefficient.

GFM-ESS incorporates a typical VSG control and replaces the DC side with an ideal DC voltage source. As shown in Fig.1, the virtual impedance control and the VFF control are introduced to improve its stability and dynamic performance. Typical voltage and current control are employed to generate the reference voltage of the bridge arm. The impedance of the inner loop in complex vector form can be written as:

$$\begin{cases} Y_{IV2+} = \dfrac{1 - f_{VF}(s) + PI_{CCL}(s)PI_{VCL}(s)}{-PI_{CCL}(s)PI_{VCL}(s)(sL_v + j\omega L_v) - sL_{f2} - PI_{CCL}(s)} \\ Y_{IV2-} = 0 \end{cases} \tag{5}$$

where L_{f2} is the filter inductance, $PI_{CCL}(s)$ and $PI_{VCL}(s)$ represent the transfer functions of the PI controllers for the current and voltage control loops, respectively. L_v is the virtual inductance, and $f_{VF}(s)$ is the transfer function of VFF control given by

$$f_{VF}(s) = \frac{k_{VF}}{1 + T_{VF}s} \tag{6}$$

where k_{VF} is the voltage feedforward coefficient and T_{VF} is the filter time constant.

C. SISO Model of the PV-ESS System

In Section II. B, impedance models in complex vector form for both devices in the local *dq* coordinate system are established. As each device employs distinct synchronization loops to track the grid phase, the PV and ESS implement vector control within their respective *dq* coordinate systems. Assuming a constant angular velocity rotation in the global

coordinate system during small perturbations, the angles by which the local coordinate systems, c_1 for GFL-PV and c_2 for GFM-ESS, deviate from the global coordinate system are expressed as:

$$\begin{cases} \Delta\theta_1 = \dfrac{1}{s}\cdot\left(k_{ppll}+\dfrac{k_{ipll}}{s}\right)\cdot\dfrac{1}{2j}\left(\Delta v_{Cdq1+,c1}-\Delta v_{Cdq1-,c1}\right) \\ \Delta\theta_2 = -\dfrac{1}{s}\cdot\dfrac{1.5V_0}{\omega_0\left(Js+D_p\right)}\cdot\dfrac{1}{2}\left(\Delta i_{dq2+,c2}+\Delta i_{dq2-,c2}\right) \end{cases} \tag{7}$$

where Δv_{Cdq1} and Δi_{dq2} are the capacitor voltage of the GFL-PV and the inductance current of the GFM-ESS, and the energy storage power fluctuation is approximated as $\Delta p=1.5V_0\cdot\Delta i_{d2,c2}$. The proportional and integral gains for the PLL are respectively denoted as k_{ppll} and k_{ipll}, while the inertia and damping coefficients for the power synchronization control (PSC) are denoted as J and D_p, respectively.

In the global coordinate system, the circuit equations for the grid side are provided by:

$$\begin{cases} \Delta v_{dq+,s} = Z_{g+}\left(\Delta i_{dq1+,s}+\Delta i_{dq2+,s}\right)+\Delta v_{gdq+,s} \\ Z_{g+} = sL_g + j\omega L_g \end{cases} \tag{8}$$

where Δv_{dq+} is the voltage of PCC, Δi_{dq1+}, and Δi_{dq2+} are the current of two converters, and Δv_{gdq+} is the voltage of the infinite bus. The grid impedance is represented by ωL_g.

Assuming a small perturbation on the phase of grid voltage and transforming (8) into the c_1 coordinate system:

$$\begin{aligned} \Delta v_{dq+,c1} = {} & Z_{g+}\left(\Delta i_{dq1+,c1}+\Delta i_{dq2+,c1}\right)-jV_{gdq+}\left(\Delta\theta_1-\Delta\theta_g\right) \\ & + jsL_gI_{gdq+}\Delta\theta_1 \end{aligned} \tag{9}$$

where V_{gdq+} and I_{gdq+} are the steady values of grid voltage and current.

$$\begin{cases} \Delta i_{dq1+,c1} = \left(1-Y_{IV1+}Z_{line1+}\right)^{-1}Y_{IV1+}\Delta v_{dq+,c1} \\ \Delta i_{dq2+,c2} = Y_{IV2+}\Delta v_{dq+,c2} \\ \Delta v_{dq+,c2} = \Delta v_{dq+,c1}+jV_{dq+}\left(\Delta\theta_1-\Delta\theta_2\right) \\ \Delta i_{dq2+,c2} = \Delta i_{dq2+,c1}+jI_{dq2+}\left(\Delta\theta_1-\Delta\theta_2\right) \end{cases} \tag{10}$$

The power angle difference between the two converters in steady state is ignored. Combining the impedance model derived in Section II. A and the relationship between different reference frames shown in (10), (9) can be further written as

$$\begin{aligned} & \left[1-Z_{g+}\left(\left(1+Y_{IV1+}Z_{line1+}\right)^{-1}Y_{IV1+}+Y_{IV2+}\right)\right]\Delta v_{dq+,c1} \\ & = jZ_{g+}\left(-I_{dq2+}+Y_{IV2+}V_{dq+}\right)\left(\Delta\theta_1-\Delta\theta_2\right)-jV_{gdq+}\left(\Delta\theta_1-\Delta\theta_g\right) \\ & \quad + jsL_gI_{gdq+}\Delta\theta_1 \end{aligned} \tag{11}$$

Furthermore, since the voltage of PCC can be expressed by the port voltage Δv_{Cdq1+} and the impedance of the GFL-PV, (11) can be rewritten as:

$$\begin{aligned} G_+\Delta v_{Cdq1+,c1} = {} & jZ_{g+}\left(-I_{dq2+}+Y_{IV2+}V_{dq+}\right)\left(\Delta\theta_1-\Delta\theta_2\right) \\ & -jV_{gdq+}\left(\Delta\theta_1-\Delta\theta_g\right)+jsL_gI_{gdq+}\Delta\theta_1 \end{aligned}$$

$$G_+ = \left[1-Z_{g+}\left(\left(1+Y_{IV1+}Z_{line1+}\right)^{-1}Y_{IV1+}+Y_{IV2+}\right)\right]\left(1-Y_{IV1+}Z_{line1+}\right)$$

(12)

Equation (12) describes how the power angle of two converters affects the port voltage of the GFL-PV. The variation in this port voltage will further influence the power angle $\Delta\theta_1$ through the PLL, forming a closed-loop process.

Substituting (7) into (12) yields:

$$-\frac{1}{f_{PLL}}\Delta\theta_1 = G_{cou2}\left(\Delta\theta_1-\Delta\theta_2\right)+G_{in1}\left(\Delta\theta_1-\Delta\theta_g\right)$$

$$\begin{cases} G_{cou2} = -\dfrac{Z_{g+}\left(-I_{dq2+}+Y_{IV2+}V_{dq+}\right)}{G_+}-\dfrac{\bar{Z}_{g+}\left(-I_{dq2-}+\bar{Y}_{IV2+}V_{dq-}\right)}{\bar{G}_+} \\ G_{in1} = \dfrac{V_{gdq+}}{G_+}+\dfrac{V_{gdq-}}{\bar{G}_+}-sL_g\left(\dfrac{I_{gdq+}}{G_+}+\dfrac{I_{gdq-}}{\bar{G}_+}\right) \\ f_{PLL} = \dfrac{PI_{PLL}}{2s} \end{cases} \tag{13}$$

The above equation provides a linear expression relating the system input $\Delta\theta_g$ to the outputs $\Delta\theta_1$ and $\Delta\theta_2$. It is noteworthy that both G_{cou2} and G_{in1} are real transfer functions, as they represent the sum of two conjugate terms.

Equations (9)-(12) are all written in the reference frame of $c1$. Similarly, the corresponding expressions in the reference frame of $c2$ can be derived to obtain another input-output relationship, which is shown in (14).

$$-\frac{1}{f_{PSC}}\Delta\theta_2 = G_{cou1}\left(\Delta\theta_2-\Delta\theta_1\right)+G_{in2}\left(\Delta\theta_2-\Delta\theta_g\right)$$

$$\begin{cases} G_{cou1} = \dfrac{jZ_{g+}\left(-I_{dq1+}+Y_{IV1+}V_{dq+}\right)}{G_+Z_{IV2+}}-\dfrac{j\bar{Z}_{g+}\left(-I_{dq1-}+\bar{Y}_{IV1+}V_{dq-}\right)}{\bar{G}_+\bar{Z}_{IV2+}} \\ G_{in2} = \dfrac{-jV_{gdq+}}{G_+Z_{IV2+}}+\dfrac{jV_{gdq-}}{\bar{G}_+\bar{Z}_{IV2+}}+sL_g\left(\dfrac{jI_{gdq+}}{G_+Z_{IV2+}}-\dfrac{jI_{gdq-}}{\bar{G}_+\bar{Z}_{IV2+}}\right) \\ f_{PSC} = \dfrac{F_{PSC}}{2s} \end{cases} \tag{14}$$

To analyze how GFM affects the stability of GFL-PV, $\Delta\theta_2$ is expressed through (14) and substituted into (13). The closed-loop SISO model for the entire PV-ESS system can be described by (15).

$$\begin{aligned} \Delta\theta_1 = {} & \frac{f_{\delta01}f_{PLL}}{1+f_{\delta1}f_{PLL}}\Delta\theta_g \\ & \begin{cases} f_{\delta1} = \underbrace{\dfrac{f_{PSC}G_{in2}+1}{f_{PSC}\left(G_{cou1}+G_{in2}\right)+1}}_{G_{out2}}G_{cou2}+G_{in1} \\ f_{\delta01} = \dfrac{f_{PSC}G_{in2}}{f_{PSC}\left(G_{cou1}+G_{in2}\right)+1}G_{cou2}+G_{in1} \end{cases} \end{aligned} \tag{15}$$

Thus, the open-loop transfer function of the system can be regarded as:

$$L_1(s) = f_{\delta1}(s)\times f_{PLL}(s) \tag{16}$$

In (16), the function $f_{\delta1}(s)$ integrates the grid structure, *LC*

This article has been accepted for publication in IEEE Transactions on Sustainable Energy. This is the author's version which has not been fully edited and content may change prior to final publication. Citation information: DOI 10.1109/TSTE.2024.3471801

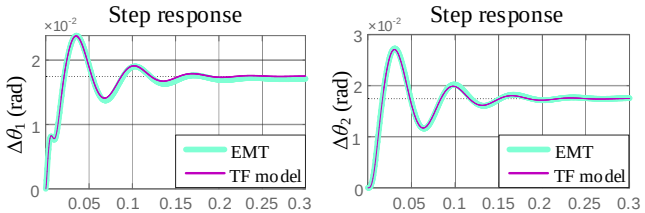

Fig. 2 Steps responses of the proposed model and EMT simulation.

filter, current control loop, and the dynamics of GFM-ESS. Meanwhile, the dynamics of the PLL are distinctly encapsulated by the function $f_{PLL}(s)$, facilitating precise parameter tuning and loop shaping.

Similarly, by formulating $\Delta\theta_1$ through (13) and substituting it into (14), the closed-loop SISO transfer function of $\Delta\theta_2$ with respect to the input $\Delta\theta_g$ can be derived. This function is employed to analyze the influence of PV on the stability of GFM-ESS.

$$\Delta\theta_2 = \frac{f_{\delta 02} f_{PSC}}{1 + f_{\delta 2} f_{PSC}} \Delta\theta_g$$

$$\begin{cases} f_{\delta 2} = \underbrace{\dfrac{f_{PLL} G_{in1} + 1}{f_{PLL}\left(G_{cou2} + G_{in1}\right) + 1}}_{G_{out1}} G_{cou1} + G_{in2} \\ f_{\delta 02} = \dfrac{f_{PLL} G_{in1}}{f_{PLL}\left(G_{cou2} + G_{in1}\right) + 1} G_{cou1} + G_{in2} \end{cases} \tag{17}$$

The corresponding open-loop transfer function is:

$$L_2(s) = f_{\delta 2}(s) \times f_{PSC}(s) \tag{18}$$

To verify the correctness and accuracy of the modeling, we compare the step responses of the closed-loop transfer function in (15) and (17) with the electromagnetic transient models in MATLAB/Simulink. As can be seen in Fig. 2, the results of the electromagnetic transient simulation are consistent with those of the proposed models, validating the accuracy.

D. Discussions on the Derived SISO model

As shown in (15) and (17), the open-loop transfer function $L_1(s)$ and $L_2(s)$ elucidate how two converters respond to the small phase perturbations in the infinite bus. This SISO model effectively captures the grid synchronization dynamics, offering insights into a spectrum of small perturbation stability concerns within the system.

In contrast to impedance models and state-space models, the proposed SISO model focuses on the phase angle response of the converter. The model utilizes the voltage and current of the converter as intermediate variables, circumventing the need for employing the generalized Nyquist criterion to analyze stability. On the other hand, the inner-loop dynamics of both converters are integrated, possess symmetrical characteristics, and are cascaded with the synchronous loop. This separation proves to be advantageous for in-depth analysis of stability mechanisms and facilitates precise tuning of controller parameters.

The proposed model simplifies the complex coupling between the two devices into a single SISO transfer function

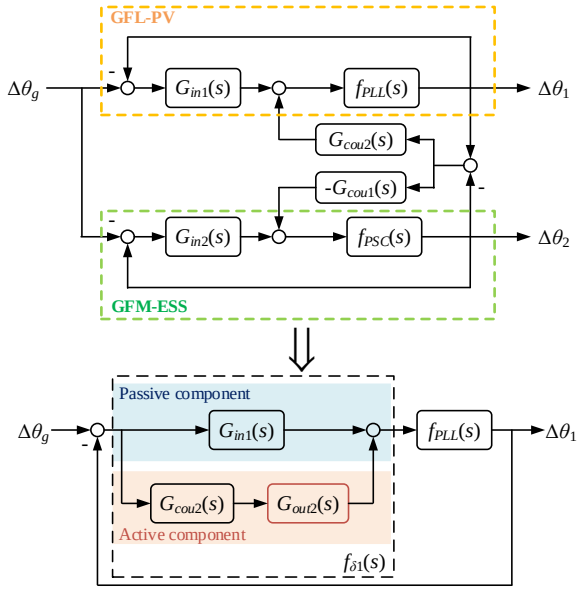

Fig. 3 SISO model of the PV-ESS system.

under the synchronous framework of GFL-PV, as illustrated in Fig. 3. The diagram represents the dominant loop of GFL-PV. Since $f_{PLL}(s)$ contains only information related to the PLL, it suffices to focus on the contributions of each component of $f_{\delta 1}(s)$ when analyzing the support mechanism of GFM.

The physical implications of the open-loop transfer function depicted in Fig. 3 are analyzed as follows. The transfer function $f_{\delta 1}(s)$ incorporates the entire dynamics of GFM-ESS, determined collectively by three components: $G_{in1}(s)$, $G_{cou2}(s)$, and $G_{out2}(s)$. Their detailed expressions are provided in (13) and (15). Among these, $G_{in1}(s)$ describes the overall behavior of the inner-loop dynamics of the two converters, encompassing the contribution of GFM to the grid voltage. This component does not involve transformations between coordinate systems but passively follows disturbances, exhibiting the characteristics of passive devices.

Examining (5), the small-signal impedance of GFM closely resembles a variable inductor when f_{VF} equals 1, as presented in (19). Hence, the physical significance of $G_{in1}(s)$ for GFL-PV is equivalent to a paralleled variable inductor to the PCC. We designate $G_{in1}(s)$ as the passive component. From another perspective, the passive component merely alters the inner loop control of GFL without providing substantial support effects.

$$\begin{cases} Z_{IV2+} \approx -\left(sL_v + j\omega L_v\right) - \dfrac{sL_{f2}}{PI_{CCL}(s) PI_{VCL}(s)} \\ Z_{IV2-} = 0 \end{cases} \tag{19}$$

From the derivation process, it is evident that the component $G_{cou2}(s)$ arises from the transformation of current vectors from the GFM coordinate system to the GFL coordinate system. In other words, due to the inherent synchronous dynamics of GFM, it suppresses the transmission of phase disturbances from the grid side to the GFL port. Consequently, $G_{cou2}(s)$ exhibits the characteristics of an active device, and we refer to it as the active component.

When $G_{cou2}(s)$ and $G_{in1}(s)$ combine, their physical

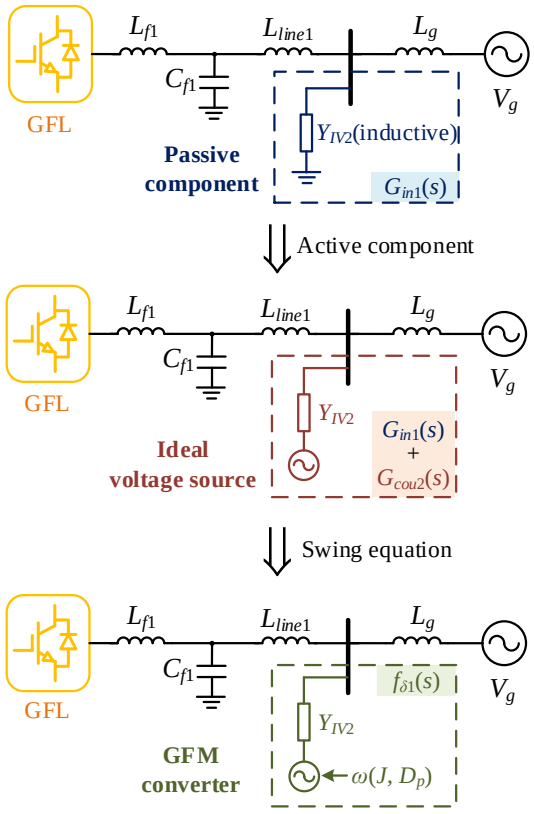

Fig. 4 physical significance of passive and active component.

interpretation is equal to a paralleled ideal voltage source with a series impedance at the PCC. This impedance corresponds to the aforementioned variable inductor. Notably, $\Delta\theta_2$ is regarded as 0 in this context, as the coordinate system of the ideal voltage source rotates at a constant angular velocity.

Furthermore, if the ideal voltage source exhibits a certain swing characteristic of power angle, it shares the same dynamics as GFM. The transfer function $G_{out2}(s)$ is utilized to depict the attenuating effect of the GFM synchronization loop on the active component. As the inertia and damping parameters of GFM increase, $G_{out2}(s)$ approaches unity. $G_{out2}(s)$ is multiplied by the active component and then added to the passive component, collectively forming the transfer function $f_{\delta 1}(s)$ to describe the support effects of GFM. The physical significance of each component is depicted in Fig. 4.

In summary, the proposed SISO model not only simplifies the process of stability analysis and parameter tuning but also provides a clear physical explanation of the supportive role of GFM-ESS on PV. It offers further insights into the interaction between the two types of converters. A detailed stability analysis will be provided in the next section.

III. Analysis of the Dynamic Interaction between GFL-PV and GFM-ESS

The open-loop transfer functions $L_1(s)$ and $L_2(s)$, derived in Section II. C, serve as crucial elements for assessing the stability of the system. The stability criterion dictates that $L_1(s)$ and $L_2(s)$ must satisfy the Nyquist stability criterion. It is

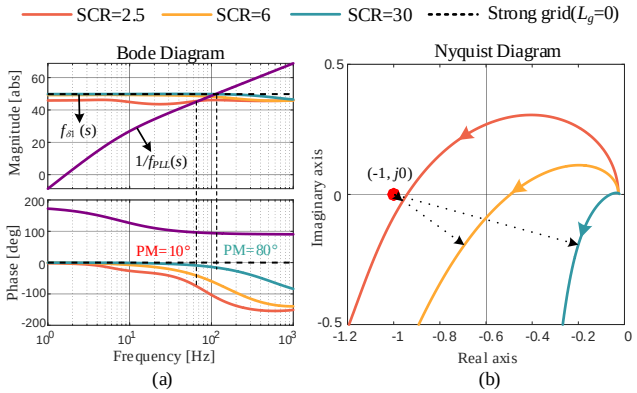

Fig. 5 PV stability analysis with different SCR. (a) Bode diagrams. (b) Nyquist diagrams.

imperative to highlight that $L_1(s)$ and $L_2(s)$ represent the open-loop transfer functions of the dominant loops of PV and ESS, respectively, allowing for the distinct characterization of the stability margins of each device. The system parameters are listed in Appendix B.

A. The Stability Characteristic of Single GFL-PV

The stability of a single GFL-PV connected to an infinite bus is considered first in this section (corresponding to Y_{IV2+}=0). Since $L_1(s)$ is the product of $f_{\delta 1}(s)$ and $f_{PLL}(s)$, the system is stable when and only when the phase difference between $1/f_{PLL}(s)$ and $f_{\delta 1}(s)$ at the crossover frequency (the frequency at which the amplitude-frequency curves intersect) is less than 180°.

Alterations in grid strength reveal a reduction in the system's stability margin. The Nyquist curve gradually converges towards the critical point -1+j0. Analyzing the Bode diagram, when integrated into a robust grid with L_g=0, $f_{\delta 1}(s)$ remains constant, maintaining a phase angle of 0. Essentially, the q-axis voltage at the PCC synchronizes with the introduced phase disturbance. Conversely, as the grid weakens, the q-axis voltage exhibits a more pronounced lag in response to phase perturbations. The $f_{\delta 1}(s)$ function demonstrates heightened negative phase characteristics in the mid to high-frequency range, intensifying the challenges faced by the PLL in achieving synchronization. Consequently, PV experiences instability in such conditions.

Furthermore, it is evident that the phase of $f_{\delta 1}(s)$ exhibits a monotonic decreasing behavior. Consequently, an increase in the bandwidth of the PLL leads to a rightward shift in the system crossover frequency, potentially resulting in a diminution of the stability margin. Concurrently, the phase of $1/f_{PLL}(s)$ undergoes a monotonic transition from 180 degrees to 90 degrees. The substantial transition frequency, corresponding to the phase-frequency curve at 135 degrees, may contribute to an augmented phase discrepancy between the two functions, potentially culminating in system instability.

B. The Dynamic Support Characteristics of GFM-ESS With Different Control Parameters

This subsection investigates how different control parameters affect the support capability of GFM. The

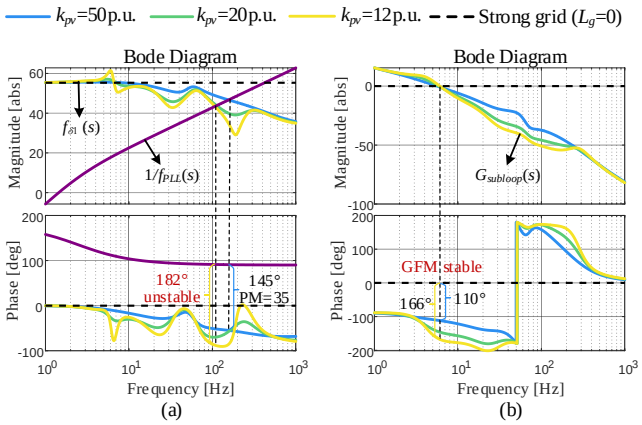

Fig. 6 Stability analysis with different voltage control gain. (a) Full-loop stability. (b) Subloop stability.

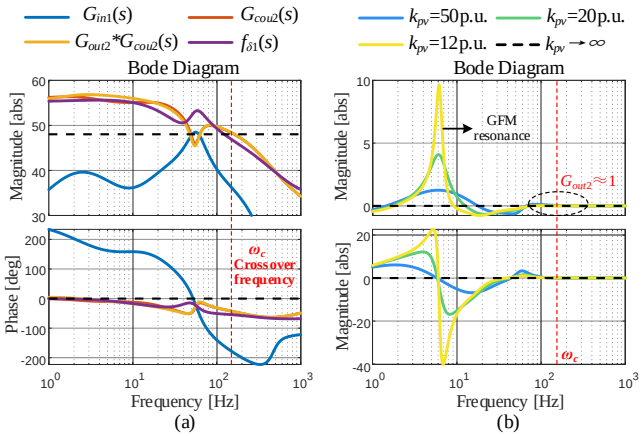

Fig. 7 Bode diagram of each component. (a) $G_{in1}(s)$, $G_{cou2}(s)$ and $f_{\delta 1}(s)$. (b) $G_{out2}(s)$.

equivalent condition for system stability is presented first referring to (15). Since the impedance of the converter itself remains stable during design, $G_{in1}(s)$ and $G_{cou2}(s)$ exhibit no right-half-plane (RHP) poles. The denominator of $G_{out1}(s)$, as well as the overall closed-loop transfer function denominator 1 + $L_1(s)$ may exhibit RHP zeros. Therefore, the system is stable if and only if the following two open-loop transfer functions satisfy the Nyquist stability criterion.

$$\begin{cases} L_1(s) = f_{\delta 1}(s) \times f_{PLL}(s) \\ G_{subloop}(s) = \left(G_{cou1}(s) + G_{in2}(s)\right) \times f_{PSC}(s) \end{cases} \tag{20}$$

Compared with (17), it is evident that $G_{subloop}(s)$ represents the dominant open-loop transfer function of the GFM when the PLL dynamics are neglected (G_{out1}=1). In other words, $L_1(s)$ will be unstable if the GFM itself becomes unstable. The instability is attributed to GFL only if the subloop transfer function $G_{subloop}(s)$ is stable while the full loop $L_1(s)$ is unstable. Therefore, the proposed model enables tracing the root cause of instability and identifying converters with lower stability margins, thereby reaffirming its superiority.

1) Influence of voltage control and VFF control

Fig. 6 illustrates the Bode diagram of the open-loop transfer functions of both the full loop and the subloop with different voltage loop proportional gain k_{pv}. As k_{pv} decreases, the subloop remains stable, albeit with decreasing stability margins. The

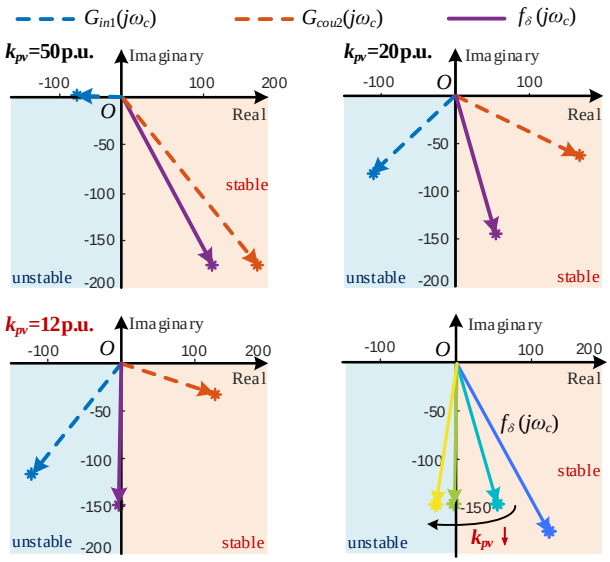

Fig. 8 Vector superposition results with different voltage control gain.

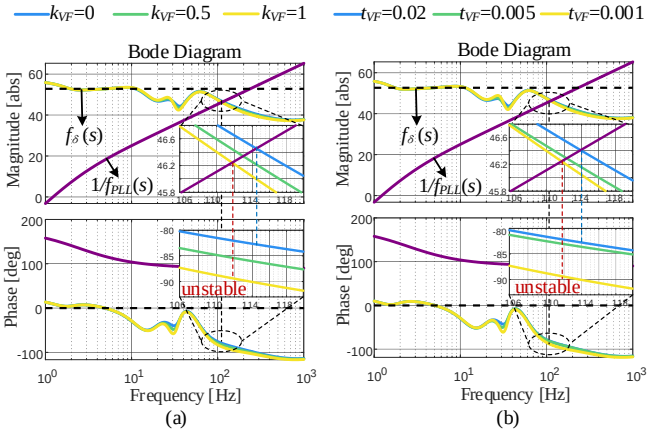

Fig. 9 Stability analysis with different VFF control. (a) voltage feedforward coefficient. (b) filter time constant.

crossover frequency of the full loop decreases, and $f_{\delta 1}(s)$ exhibits a more negative phase. When k_{pv} equals 12 p.u., $f_{\delta 1}(s)$ and $1/f_{PLL}(s)$ reach a phase difference of 182°, leading to GFL instability. It is evident that the proportional gain of the voltage loop significantly influences the stability of both converters, with larger voltage loop proportional gain enhancing the stability of the two converters.

Fig. 7 depicts the Bode diagram of the components constituting $f_{\delta 1}(s)$ when k_{pv} equals 50 p.u.. A necessary condition for system stability is that the phase of $f_{\delta 1}(s)$ is greater than -90°, with the minimum phase of $1/f_{PLL}(s)$ being 90°. Nearby the crossover frequency of the system, the phase of the passive component $G_{in1}(s)$ approaches -180°, while the phase of the active component $G_{cou2}(s)$ lies between -90° and 0°. Hence, the passive component has negative damping effects while the active component exhibits positive damping characteristics. Additionally, it is noteworthy that the effect of $G_{out2}(s)$ is concentrated in the low-frequency range, approximately equal to 1 near the crossover frequency. Therefore, the stability of the

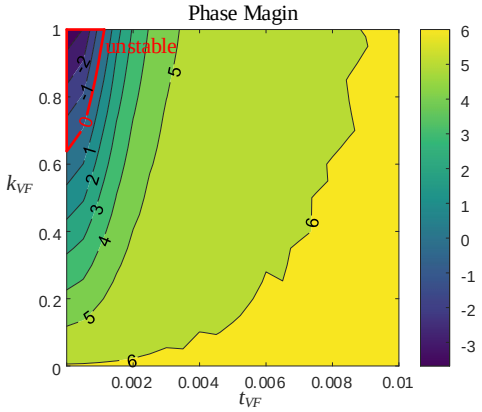

Fig. 10 Phase margin contour lines with different VFF control parameters.

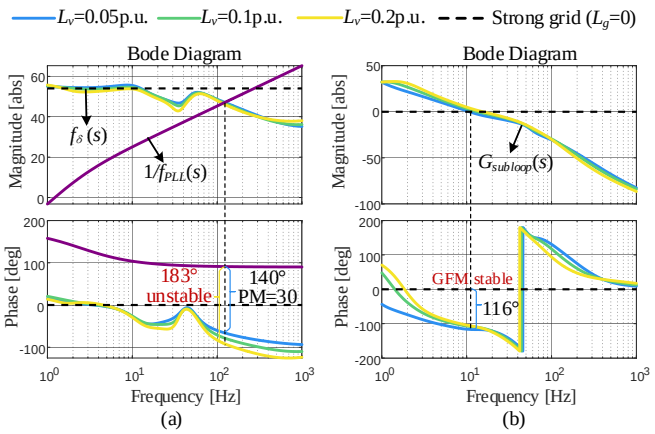

Fig. 11 Stability analysis with different virtual impedance. (a) Full loop stability. (b) Subloop stability.

system is determined by the combined influence of the active and passive components.

Fig. 8 illustrates the vector addition effects with different voltage control parameters, providing a clearer explanation of the instability phenomenon. When k_{pv} equals to 50 p.u., the active component dominates due to its larger magnitude, resulting in the synthesized $f_{\delta 1}(s)$ falling within the positive damping region, ensuring system stability. As k_{pv} decreases, the passive component rotates towards the positive damping region, while the magnitude of the active component decreases and that of the passive component increases. Eventually, the passive component predominates, leading to system instability.

Compared to voltage vector control, voltage feedforward control exhibits a relatively minor impact on the stability of GFL. Fig. 9 illustrates the Bode diagram of $1/f_{PLL}(s)$ and $f_{\delta 1}(s)$ with different voltage feedforward coefficients k_{VF} and filtering time constants T_{VF}. The stability margin of GFL decreases with increasing k_{VF} or decreasing T_{VF}. To visually represent their effects, Fig. 10 presents contour plots of the stability margin as a function of k_{VF} and T_{VF}. It is evident that VFF control, while enhancing the dynamic performance of GFM itself, also introduces certain adverse effects on its support capability.

2) Influence of virtual impedance control

Virtual impedance is commonly employed to mitigate sub-synchronous oscillations of GFM converters in strong grids. By

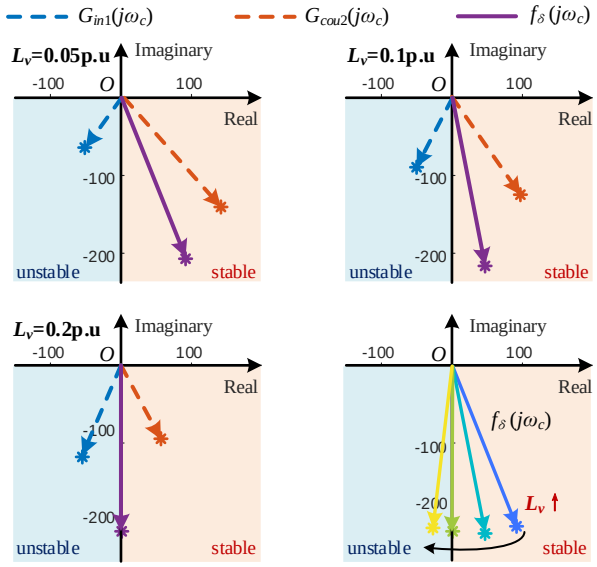

Fig. 12 Vector superposition results with different virtual impedance.

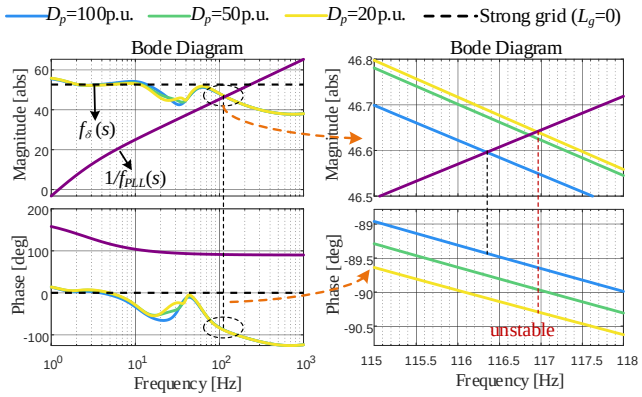

Fig. 13 Stability analysis with different damping coefficient.

introducing additional control, it increases the electrical distance between two voltage sources. Clearly, this also affects the support characteristics of GFM. Fig. 11 depicts the Bode diagram of $1/f_{PLL}(s)$ and $f_{\delta 1}(s)$ with different virtual impedance. With the increase in virtual impedance, the support capability of GFM weakens, and the phase of $f_{\delta 1}(s)$ decreases in the mid-to-high frequency range. GFL is unstable when L_v equals 0.2 p.u., with the full loop unstable while the subloop remains stable.

Fig. 12 illustrates the vector relationship between the active and passive components with different virtual impedances. The increase in virtual impedance leads to a decrease in the magnitude of the active component and an increase in the magnitude of the passive component, causing the synthesized vector $f_{\delta 1}(j\omega_c)$ to rotate toward the negative damping region. Unlike reducing the proportional gain coefficient of the voltage loop, the phase of the active component also gradually decreases. This suggests that virtual impedance may have a more significant impact on the support capability of GFM.

3) Influence of power synchronization control

Power synchronous control introduces frequency swing characteristics to GFM, enabling it to regulate active power. Fig.

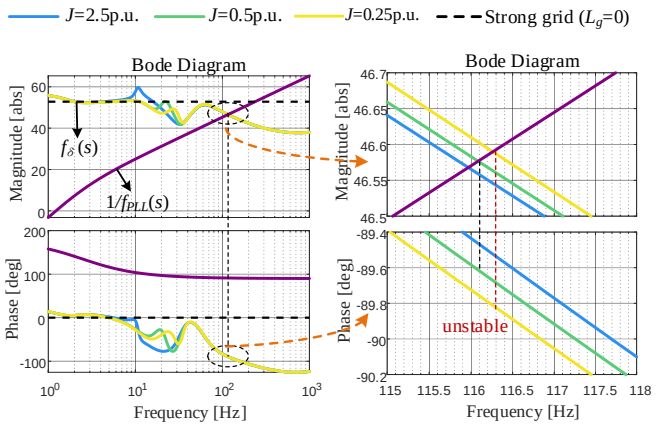

Fig. 14 Stability analysis with different inertia coefficient.

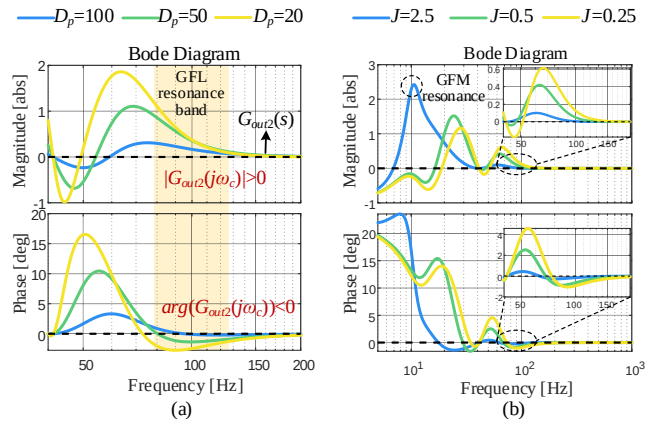

Fig. 15 Bode diagram of $G_{out2}(s)$. (a) different damping coefficient. (b) inertia coefficient.

13 and Fig. 14 respectively presents the Bode diagram of the open-loop transfer function under different virtual damping D_p and inertia parameters J. Due to the low bandwidth of the PSC, reducing J or D_p results in a slight decrease in the stability margin of GFL. GFL becomes unstable when D_p equals 20 p.u. in Fig. 13, and instability occurs when J decreases to 0.25 p.u. in Fig. 14. It is evident that the swing equation slightly diminishes the support capability of GFM.

In the preceding analysis, the effects of PSC have been attributed to the transfer function $G_{out2}(s)$ while being independent of other components. Fig. 15 depicts the Bode diagram of $G_{out2}(s)$ for varying values of J and D_p. Within the oscillatory frequency range of GFL (around 100Hz in this case), $G_{out2}(s)$ exhibits characteristics of positive magnitude and negative phase, which become more pronounced with decreasing values of J and D_p. This phenomenon not only reduces the phase of the active components but also causes a slight rightward shift in the crossover frequency point, further diminishing the stability margin of the system.

In summary, the influence of control parameters on the support capability of GFM can be summarized as follows. The introduction of VFF control and virtual impedance control partially diminishes the support capability of GFM. Moreover, faster voltage control dynamics and slower PSC dynamics correspond to stronger support capabilities of GFM. Reflecting to (5), it becomes evident that all measures aimed at enhancing

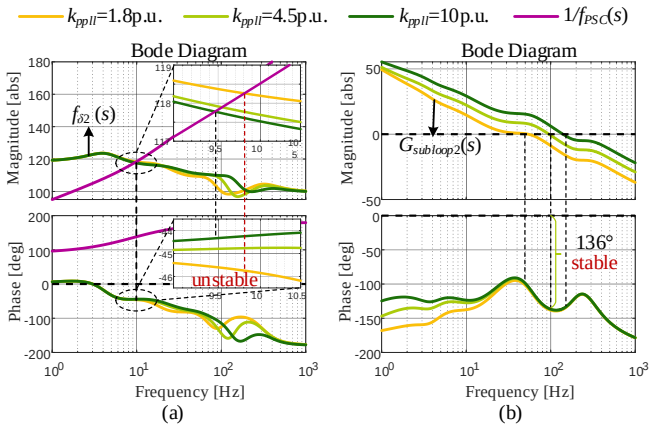

Fig. 16 Stability analysis with different PLL proportional gain. (a) Full loop stability. (b) Subloop stability.

the stability of GFL correspond to an increase in the inner loop admittance of GFM. From (13), it is clear that increasing the inner loop admittance amplifies the active components while reducing the passive components, thus promoting the stability of GFL.

C. The Impact of GFL-PV on the Stability of GFM-ESS

The PV station operating in GFL mode injects power into the grid as a current source. In small-signal stability analysis of power systems, an ideal current source can be considered as an open circuit. However, due to the dynamic nature of the current control loop, GFL-PV cannot be treated as an ideal current source, leading to interactions with GFM-ESS. In the following analysis, the transfer functions derived in (17) are used to assess the impact of GFL-PV on the stability of GFM-ESS.

As mentioned in Section III. B, $G_{in1}(s)$ and $G_{cou2}(s)$ exhibit no RHP poles since the impedance of the converter itself is stable. However, the denominator of $G_{out2}(s)$, as well as $1 + L_2(s)$ may potentially exhibit RHP zeros. The system is stable if both the following open-loop transfer functions satisfy the Nyquist stability criterion.

$$\begin{cases} L_2(s) = f_{\delta 2}(s) \times f_{PSC}(s) \\ G_{subloop2}(s) = \left(G_{cou2}(s) + G_{in1}(s)\right) \times f_{PLL}(s) \end{cases} \tag{21}$$

The transfer function $L_2(s)$ in (21) reflects the stability of GFM, taking into account the influence of GFL, while $G_{subloop2}(s)$ characterizes the stability of the GFL without considering the dynamics of the PSC. If $G_{subloop2}(s)$ is stable while $L_2(s)$ is unstable, it indicates that the instability of the system stems from the GFM.

1) Effects of PLL

Fig. 16 illustrates the Bode diagram of $f_{\delta 2}(s)$ and $G_{subloop2}(s)$ for different values of the proportional gain k_{ppll} of the PLL. Since the sub-loop remains stable, any instability observed in $L_2(s)$ is attributed to the GFM. In combination with the characteristics of $1/f_{PSC}(s)$, it is evident that the stability margin of the GFM decreases as k_{ppll} decreases. This suggests that a PLL with slower dynamics interacts more significantly with the GFM, thereby reducing its stability.

Similarly, Fig. 17 illustrates the Bode diagram of the

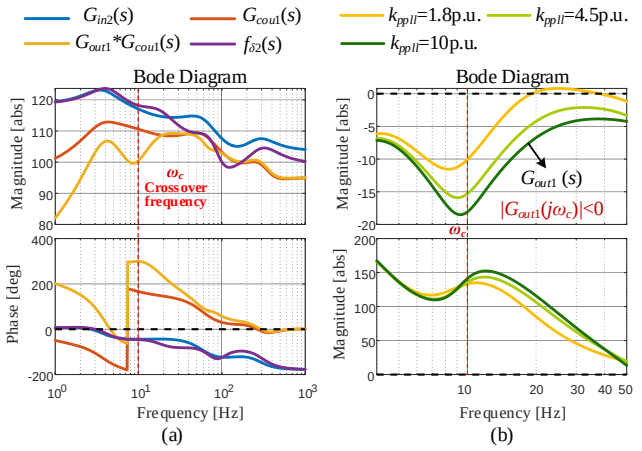

Fig. 17 Bode diagram of each component. (a) G_{in2}(s), G_{cou1}(s) and $f_{\delta 2}$(s). (b) G_{out1}(s).

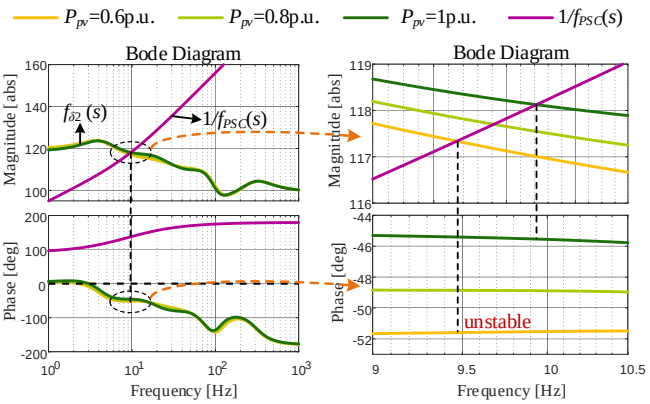

Fig. 18 Stability analysis with different active power of PV.

components that constitute $f_{\delta 2}(s)$. The passive component $G_{in2}(s)$ has a predominant influence on $f_{\delta 2}(s)$, indicating the potential utilization of passive devices to emulate GFL effects. The active component $G_{cou1}(s)$ slightly amplifies the magnitude of $f_{\delta 2}(s)$, negatively affecting the stability of the GFM. Additionally, $G_{out1}(s)$ characterizes the action of the PLL, showing a negative magnitude near the crossover frequency of the GFM, thereby attenuating the influence of the active component.

2) Effects of PV output

The output of PV system exhibit randomness and fluctuation, which can also affect the stability of GFM. Fig. 18 illustrates the Bode diagram of $1/f_{PSC}(s)$ and $f_{\delta 2}(s)$ under different PV outputs. As the PV output decreases, the phase of $f_{\delta 2}(s)$ also decreases. When the active power of PV drops to 0.6 p.u., the phase difference between $1/f_{PSC}(s)$ and $f_{\delta 2}(s)$ reaches 184°, indicating system instability. Therefore, while the GFM provides dynamic support to the PV, the power output from the PV also mitigates the sub-synchronous oscillations of the GFM to some extent. This mutual interaction promotes system stability.

D. Summary of Influencing Patterns

Based on the stability analysis in this section, the interaction patterns between the GFM-ESS and GFL-PV are summarized in Fig. 19. The red arrows in the figure indicate that a decrease

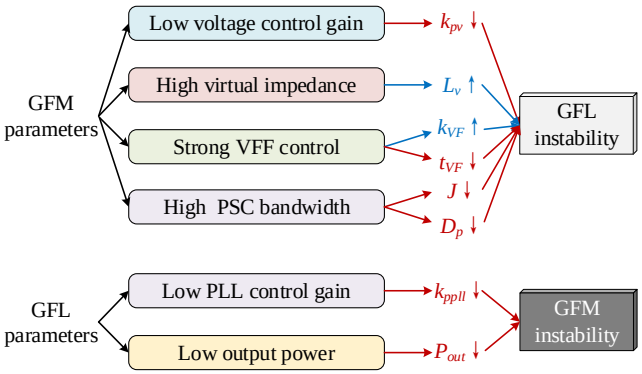

Fig. 19 Summary of interactions with different parameters.

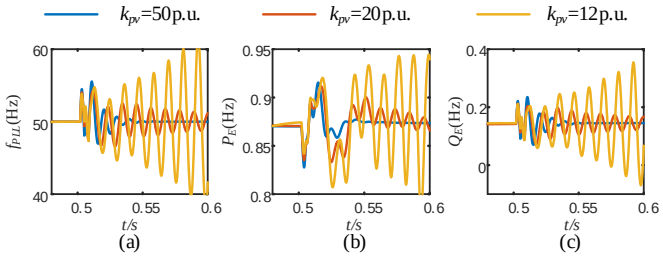

Fig. 20 Simulation results with different voltage control loop proportional gain. (a) PLL output frequency. (b) Active power. (c) Reactive power.

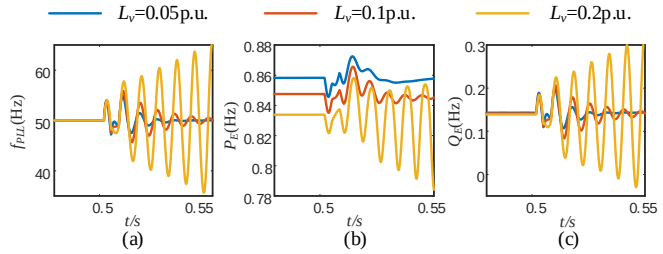

Fig. 21 Simulation results with different virtual impedance. (a) PLL output frequency. (b) Active power. (c) Reactive power.

in the specified parameter reduces the stability of the other device, whereas the blue arrows represent the opposite effect. This figure provides a comprehensive understanding of the mutual interaction patterns between the two types of converters.

IV. Simulation And Experiment Validation

A. Simulation Results

To validate the proposed stability analysis, electromagnetic transient simulations of the PV-ESS system are conducted in MATLAB/Simulink. This study focuses on assessing the interaction between the PV system and the ESS under various parameter configurations.

Assuming a grid weakening event caused by a line outage, the SCR undergoes a sudden transition from 4 to 2.5 at t = 0.5s. Figs. 20 and 21 respectively illustrate the time-domain waveforms of the PLL output frequency, as well as the active and reactive power outputs of the PV system, under different voltage loop proportional gains and virtual impedances. As k_{pv} decreases from 50 p.u. to 12 p.u., the PLL output frequency and the power of the PV system exhibit oscillatory divergence

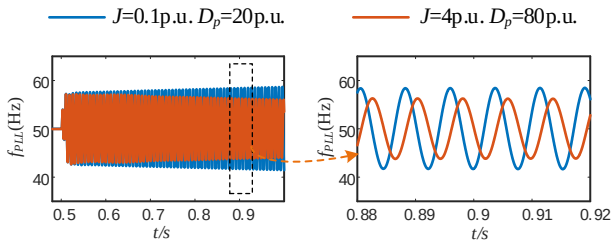

Fig. 22 Simulation results with different inertia and damping coefficient.

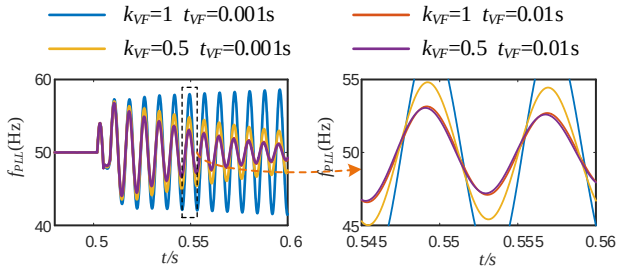

Fig. 23 Simulation results with different VFF control parameters.

around 100Hz. A similar instability occurs when the virtual impedance increases to 0.2 p.u. within the same frequency range. Under weak grid conditions, it is necessary to increase the bandwidth of the voltage loop and decrease the virtual impedance to enhance the support of the ESS for PV.

Fig. 22 illustrates the cases where smaller inertia and damping coefficients lead to system instability. When the inertia and damping of the GFM decrease to 0.1 p.u. and 20 p.u. respectively, the output frequency of the PLL diverges, aligning with the previous frequency domain analysis. Consequently, the swing dynamics of the GFM slightly diminish its support capability.

The impact of VFF control on the stability of the GFL is depicted in Fig. 23. The weakest stability of the GFL is observed when k_{VF} equals to 1 and t_{VF} equals 0.001, resulting in system instability. Increasing t_{VF} or decreasing k_{VF} improves the stability of the system. Additionally, when t_{VF} equals 0.01, variations in k_{VF} have minimal effect on stability, as corresponding to the results in Fig. 10. These findings demonstrate that VFF control of the GFM negatively impacts the stability of the GFL.

The following analysis validates the impact of PV on the stability of the GFM. Assuming a grid strengthening due to a short-circuit fault, SCR undergoes a step change from 2.5 to 4 at t = 0.5 s. Fig. 24 illustrates the time-domain waveforms of the PSC output frequency, along with the active and reactive power outputs of the ESS, under various PLL proportional gain coefficients. When the proportional gain of the PLL decreases to 1.14 p.u., the output frequency of the PSC begins to diverge. This indicates that a reduction in PLL bandwidth may lead to stronger interactions with the low-frequency control loop of the GFM.

Similarly, Fig. 25 illustrates the system output waveforms under different PV outputs. The system becomes unstable when the active power of PV drops to 0.4 p.u., while stability is maintained when the PV operates with an active power of 1.0

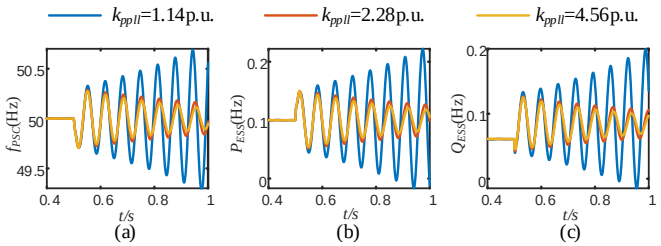

Fig. 24 Simulation results with different PLL proportional gain. (a) PSC output frequency. (b) Active power. (c) Reactive power.

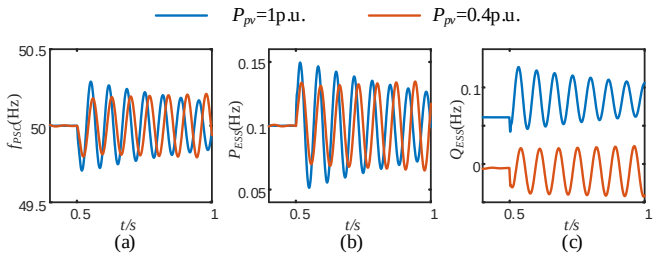

Fig. 25 Simulation results with different active power of PV. (a) PSC output frequency. (b) Active power. (c) Reactive power.

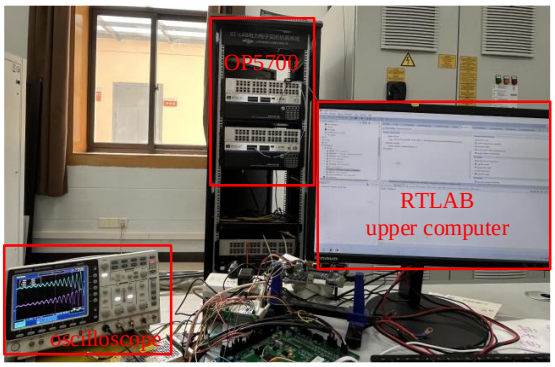

Fig. 26 RTLAB real-time simulator experiment platform

p.u. This suggests that the negative damping introduced by the integration of PV systems has a stabilizing effect on the GFM. These simulation results are consistent with the analytical findings derived from the developed small-signal model.

B. Experiment Results

To verify the effectiveness of the theoretical analysis, experimental validations have been conducted in a laboratory setup. The PV-ESS system depicted in Fig. 1 is constructed on the real-time simulation experiment platform RTLAB, as illustrated in Fig. 26. The simulator employs the OP5700 from OPAL-RT, with analog output (AO) boards connected externally to an oscilloscope for real-time waveform monitoring. In cases 1 to 3, the system's SCR is set to 2.5, with the aim of verifying scenarios where GFM parameters lead to instability in GFL. On the other hand, in case 4, the SCR is set to 4.5 to examine the instability caused by GFM.

Case 1 validates the influence of GFM voltage control and virtual impedance control on the stability of GFL. The experimental results are shown in Fig. 27. At 0.5s, a line fault causes an increase in the connection lines of GFL, leading to a

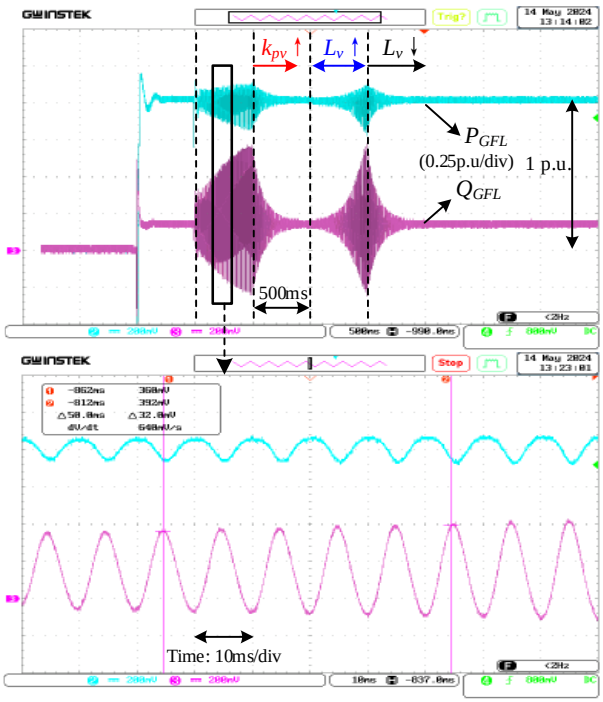

Fig. 27 Experiment results with changed voltage control proportional gain and virtual impedance.

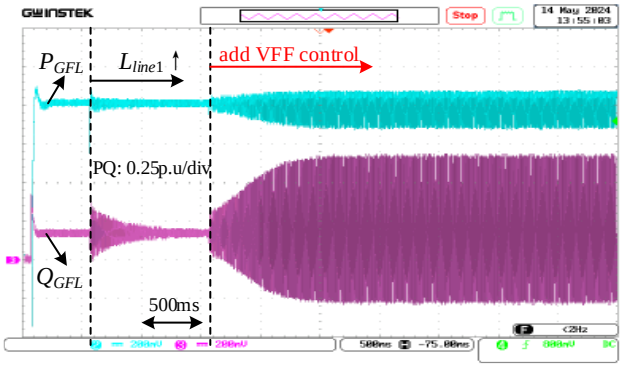

Fig. 28 Experiment results after introducing VFF control.

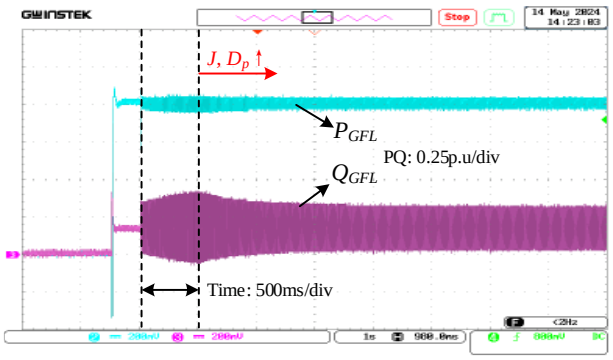

Fig. 29 Experiment results with changed inertia and damping coefficient.

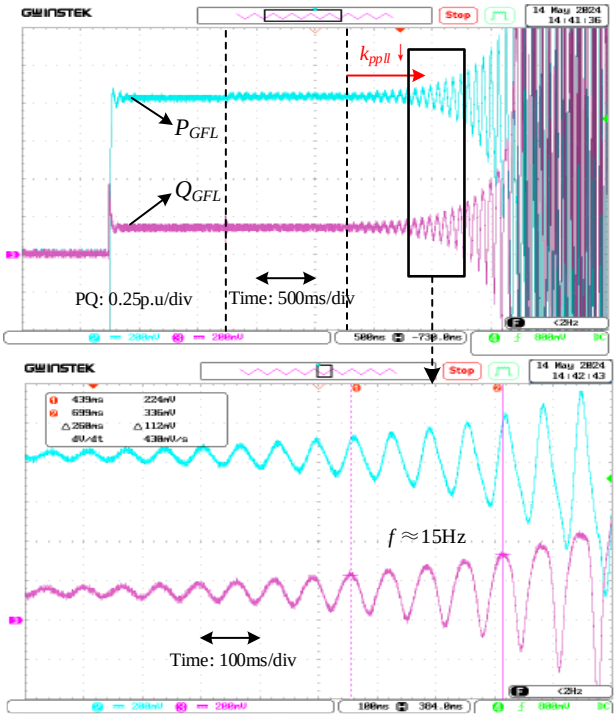

Fig. 30 Experiment results with changed PLL proportional gain.

divergence in GFL output power. The observed oscillation frequency is around 100Hz, predominantly governed by GFL. At 1s, increasing the voltage control gain of GFM results in waveform convergence, confirming the positive impact of higher voltage control gain on the system stability. At 1.5s, introducing a virtual impedance control of 0.05p.u. by GFM destabilizes the system. At 2s, removing the virtual impedance control restores system stability, confirming the attenuating effect of virtual impedance on the stability of GFL.

The experiment result of Case 2 is presented in Fig 28. The system remains stable after experiencing the line fault disturbance. At 1.5s, voltage feedforward control is implemented by GFM, precipitating system instability. This verifies the adverse effect of voltage feedforward control by GFM on the stability of GFL.

In Case 3, the system experiences instability following a line fault disturbance. At 1.5s, the inertia of GFM is increased from 0.2 p.u. to 2 p.u. and the damping coefficients are increased from 10 p.u. to 40 p.u., causing the output power of GFL to transition from divergence to convergence in Fig. 29. This validates the role of inertia and damping coefficients in stabilizing the GFL.

Fig. 30 presents the experiment result of Case 4, where the impact of GFL's PLL parameters on the stability of GFM is examined. At 1s, a reduction in GFM connection lines induces system oscillations, which are followed by convergence. The observed oscillation frequency is around 15Hz, with this mode being predominantly governed by the GFM. At 1.5s, the proportional gain of the PLL is decreased from 4.5 p.u. to 1.2 p.u., leading to a divergence in GFM's output power. This confirms that reduced PLL parameters can compromise the stability of the GFM.

V. Conclusion

This paper presents a SISO small-signal model for the hybrid system consisting of GFL-PV and GFM-ESS. Based on

this model, it offers clear explanations of the dynamic behaviors and physical mechanisms underlying their interactions. The influence of multiple control parameters in GFM on the stability of GFL is thoroughly investigated. Furthermore, the quantification of stability margins with different control parameters for both converters provide further insights into the stability analysis and parameter tuning of the system. The main conclusions are summarized as follows.

1) The voltage loop in GFM-ESS emerges as the primary interface for interaction with GFL-PV. An increase in the proportional gain of the voltage control not only enhances the stability of GFM but also proves advantageous in enhancing the robustness source characteristics of GFM, thereby improving the stability of GFL. Additionally, it has been found that the voltage feedforward control of GFM can have a certain negative impact on the stability of GFL. Larger voltage feedforward gain and smaller filter time constants may lead to instability in GFL.
2) Increasing the virtual impedance enhances the stability of the ESS under strong grid conditions. However, it leads to an opposing impact on the stability of PV. The selection of virtual impedance values depends on the SCR. An increase in the inertia and damping coefficients of GFM leads to a slight improvement in the stability of GFL. However, larger inertia coefficients may induce sub-synchronous oscillations within GFM itself.
3) Similarly, the stability of GFM is also influenced by the GFL converters. The renewable energy sources from GFL may introduce negative damping to the grid; however, this negative damping can help suppress oscillations in the GFM within the hybrid system. Additionally, it has been observed that reducing the proportional gain of the PLL may increase interactions with the low-frequency control loop of GFM, potentially leading to instability.

APPENDIX A
ADMITTANCE MODEL OF GFL AND GFM CONVERTERS

The admittance model of the GFL and GFM converter is derived based on the complex vectors. In the controller's rotating *dq*-frame (determined by PLL and PSC), the *LC* filters' equations are expressed as:

$$\begin{aligned} u_{dq+}^{*} - v_{dq+} &= \left(sL_{f1} + j\omega L_{f1}\right) i_{Ldq+} \\ i_{Ldq+} - i_{dq+} &= \left(sC_{f1} + j\omega C_{f1}\right) v_{dq+} \end{aligned} \tag{A.1}$$

where u_{dq+}^{*}, v_{dq+}, i_{Ldq+}, and i_{dq+} are the corresponding vectors of the reference voltage, output voltage, inductance current, and output current in the controller's *dq*-frame. All complex vector has forms: $x_{dq+}=x_d + jx_q$.

The control law of the current control loop is

$$u_{dq+}^{*} = PI_{CCL}(s)\left(i_{dqref+} - i_{Ldq+}\right) + j\omega L_{f1} i_{Ldq+} + k_F v_{dq+} \tag{A.2}$$

where i_{dqref+} is the reference current and can be treated as 0 when the DC voltage control is ignored.

By combining (A.1) and (A.2), the admittance model of the inner loop for GFL converters can be obtained, as shown in (4). The component Y_{IV-} equals zeros due to the symmetric condition.

$$Y_{IV1+} = v_{dq+} / i_{dq+}, \quad Y_{IV1-} = 0 \tag{A.3}$$

For the GFM converter, the circuit equations are the same as (A.1), and the control law of the voltage and current control can be written as

$$\begin{aligned} u_{dq+}^{*} &= PI_{CCL}(s)\left(i_{dqref+} - i_{Ldq+}\right) + j\omega L_{f2} i_{Ldq+} + f_{VF}(s) v_{dq+} \\ i_{dqref+} &= PI_{VCL}(s)\left(v_{vdqref+} - v_{dq+}\right) + j\omega C_{f2} v_{dq+} \end{aligned} \tag{A.4}$$

where $v_{vdqref+}$ is the voltage reference generated by virtual impedance, the control law of the virtual impedance is

$$v_{vdqref+} = v_{dqref+} - \left(sL_v + j\omega L_v\right) i_{dq+} \tag{A.5}$$

When the constant voltage control is adopted by the GFM converter, v_{dqref+} can be regarded as zeros. Combining (A.1), (A.4), (A.5) and ignoring the dynamic of the capacitance, the admittance model of the GFM's inner loop can be derived. The final result can be seen in (5).

APPENDIX B

Table I
PARAMETERS OF THE PV-ESS SYSTEM

The base value for per-unit calculation		
f_{Base}=50Hz	S_{Base}=100MW	V_{Base}=380V
System parameters		
PV line inductance	L_{line1}	0.15p.u.
ESS line inductance	L_{line2}	0.01p.u.
grid inductance	L_g	0.4p.u.
Control parameters of GFL-PV		
DC voltage control	k_{pdc}	2.5 p.u.
	k_{idc}	80 p.u.
PLL control	k_{ppll}	2.3 p.u.
	k_{ipll}	35p.u.
Current control	k_{pc}	0.4 p.u.
	k_{ic}	30 p.u.
Voltage feedforward control	k_F	0.5
Control parameters of GFM-ESS		
PSC	J	0.5 p.u.
	D_p	65 p.u.
Voltage control	k_{pv}	30 p.u.
	k_{iv}	500 p.u.
Voltage feedforward control	k_{VF}	1
	t_{VF}	0.001

REFERENCES

[1] Z. Li and M. Shahidehpour, "Small-signal modeling and stability analysis of hybrid AC/DC microgrids," *IEEE Trans. Smart Grid*, vol. 10, no. 2, pp. 2080–2095, Mar. 2019.
[2] P. S., P. P., and B. F., "An Overview on the Reliability of Modern Power Electronic Based Power Systems," *IEEE Open J. Power Electron.*, vol. 1, pp. 34-50, 2020.
[3] D. W., X. H., W. D., and H. L., "Small Signal Stability Analysis of Multi-Infeed Power Electronic Systems Based on Grid Strength Assessment," *IEEE Trans. Power Syst.*, vol. 34, no. 2, pp. 1393-1403, 2019.
[4] F. J., L. H., T. Y., and B. F., "On the Inertia of Future More-Electronics Power Systems," *IEEE J. Emerg. Sel. Top. Power Electron.*, vol. 7, no. 4, pp. 2130-2146, 2019.
[5] P. Q., J. Q., Y. Y., L. T., W. H., and B. F., "On the Stability of Power Electronics-Dominated Systems: Challenges and Potential Solutions," *IEEE Trans. Ind. Appl.*, vol. 55, no. 6, pp. 7657-7670, 2019.

[6] X. Wang and F. Blaabjerg, "Harmonic stability in power electronic based power systems: concept, modeling, and analysis," *IEEE Trans. Smart Grid*, vol. 10, no. 3, pp. 2858–2870, May 2019.
[7] National Grid, "Performance of phase-locked loop based converters," System Operability Framework, U.K., Tech. Rep., Dec. 2017.
[8] L. R., Y. J., W. X., S. P., P. J., and H. J., "Dynamic Stability Analysis and Improved LVRT Schemes of DFIG-Based Wind Turbines During a Symmetrical Fault in a Weak Grid," *IEEE Trans. Power Electron.*, vol. 35, no. 1, pp. 303-318, 2020.
[9] W. D., L. L., S. L., H. J., and H. Y., "Analysis of Modal Resonance Between PLL and DC-Link Voltage Control in Weak-Grid Tied VSCs," *IEEE Trans. Power Syst.*, vol. 34, no. 2, pp. 1127-1138, 2019.
[10] R. Rosso, X. Wang, M. Liserre, X. Lu, and S. Engelken, "Grid-forming converters: An overview of control approaches and future trends," in Proc. IEEE Energy Convers. Congr. Expo., Detroit, MI, 2020, pp. 4292– 4299.
[11] L. Zhang, L. Harnefors, and H. P. Nee, "Power synchronization control of grid-connected voltage source converters," *IEEE Trans. Power Syst.*, vol. 25, no. 2, pp. 809–820, May 2010.
[12]Ma F, Xin H, Wu D, et al. Assessing Grid Strength of 100% Inverter-Based Power Systems[J]. 2023.
[13]W. X., G. T. M., W. H., L. Y., B. F., and H. L., "Grid-Synchronization Stability of Converter-Based Resources—An Overview," *IEEE Open Journal of Industry Applications*, vol. 1, pp. 115-134, 2020.
[14]J. A. Suul, S. D'Arco, P. Rodríguez, and M. Molinas, "Impedance compensated grid synchronization for extending the stability range of weak grids with voltage source converters," *IET Gener. Transm. Distrib.*, vol. 10, no. 6, pp. 1315–1326, Apr. 2016.
[15]H. F., Z. X., L. M., L. F., and Z. W., "Stability Control for Grid-Connected Inverters Based on Hybrid-Mode of Grid-Following and Grid-Forming," *IEEE Trans. Ind. Electron.*, pp. 1-11, 2023.
[16]Z. H., X. W., L. W., and W. J., "Grid Forming Converters in Renewable Energy Sources Dominated Power Grid: Control Strategy, Stability, Application, and Challenges," *J. Mod. Power Syst. Clean Energy*, vol. 9, no. 6, pp. 1239-1256, 2021.
[17]L. Zhang, L. Harnefors, and H.-P. Nee, "Power-Synchronization Control of Grid-Connected Voltage-Source Converters," IEEE Trans. Power Electron., vol. 25, no. 2, pp. 809–820, May 2010.
[18]L. Harnefors, M. Hinkkanen, U. Riaz, F. M. M. Rahman, and L. Zhang, "Robust Analytic Design of Power-Synchronization Control," IEEE Trans. Ind. Electron., vol. 66, no. 8, pp. 5810–5819, Aug. 2019.
[19]G. X., Z. D., A. A., and B. F., "Stability Analysis of Grid-Following and Grid-Forming Converters Based on State-Space Model," in *2022 International Power Electronics Conference (IPEC-Himeji 2022- ECCE Asia)*, 2022, pp. 422-428.
[20]Y. W., S. S., G. V., and W. G. D., "Sequence Impedance Modeling of Grid-Forming Inverters," in *2021 IEEE Power & Energy Society General Meeting (PESGM)*, 2021, pp. 1-5.
[21]Henderson C, Egea-Alvarez A, Xu L. Analysis of multi-converter network impedance using MIMO stability criterion for multi-loop systems[J]. Electric Power Systems Research, 2022, 211: 108542.
[22]Z. Z. *et al.*, "Modeling and Control of a Two-Bus System With Grid-Forming and Grid-Following Converters," *IEEE J. Emerg. Sel. Top. Power Electron.*, vol. 10, no. 6, pp. 7133-7149, 2022.
[23]S. Jiang and G. Konstantinou, "Generalized impedance model and interaction analysis for multiple grid-forming and grid-following converters," *Electr. Power Syst. Res.*, vol. 214, p. 108912, 2023.
[24]S. P., X. H., Y. J., C. Y., H. S., and C. J., "Dynamic Interaction Analysis and Damping Control Strategy of Hybrid System With Grid-Forming and Grid-Following Control Modes," *IEEE Trans. Energy Convers.*, vol. 38, no. 3, pp. 1639-1649, 2023.
[25]Z. F. *et al.*, "Control Interaction Modeling and Analysis of Grid-Forming Battery Energy Storage System for Offshore Wind Power Plant," *IEEE Trans. Power Syst.*, vol. 37, no. 1, pp. 497-507, 2022.
[26]H. L., X. H., L. Z., J. P., Y. H., L. Z., and W. Z., "Grid-Synchronization Stability Analysis and Loop Shaping for PLL-Based Power Converters With Different Reactive Power Control," IEEE Trans. Smart Grid, 11, pp. 501-516, (2020).
[27]Y. Li, Y. Gu, Y. Zhu, A. Junyent-Ferre, X. Xiang, and T. C. Green, "Impedance Circuit Model of Grid-Forming Inverter: Visualizing Control Algorithms as Circuit Elements," IEEE Trans. Power Electron., 36, pp. 3377-3395, (2021).

Kezan Zhang received the B.Eng. degree in electrical engineering in 2022 from the Huazhong University of Science and Technology, Wuhan, China, where he is currently working toward the Ph.D. degree in electrical engineering. His research interests include modeling and control technologies of energy storage system, and renewable energy stability analysis.

Mengxuan Shi received the Ph.D. degree from Huazhong University of Science and Technology, Wuhan, China, in 2021. She is currently with Central China Branch of State Grid Corporation of China. Her research interests include large power grid stability analysis and operation control, distributed generation, and energy storage technologies.

Xia Chen received the B.S. degree in power system and its automaton from Wuhan University of Technology, China, in 2006, and the M.S. and Ph.D. degrees in electrical engineering from Huazhong University of Science and Technology (HUST), China, in 2008 and 2012, respectively. She was a Post-Doctoral Research Fellow with the University of Hong Kong, from 2012 to 2015. Now she is a professor with the School of Electrical and Electronic Engineering, HUST. Her research interests include energy storage control and operation, renewable energy integration technologies, and new smart grid device.

Dejun Shao received the Ph.D. degree from Huazhong University of Science and Technology, Wuhan, China, in 2009. He is currently with Central China Branch of State Grid Corporation of China. His research interests include large power grid stability analysis and operation control, large power grid failure defense, power grid protection.

Youping Xu received the M.S. degree from Huazhong University of Science and Technology, Wuhan, China, in 1996. He is currently with Central China Branch of State Grid Corporation of China. His research interests include large power grid stability analysis and operation control, large power grid failure defense.

Yin Chen received the B.S. degree in electrical engineering from Huazhong University of Science and Technology, Wuhan, China, in 2009, and the M.S. degree in electrical engineering from Zhejiang University, Hangzhou, China, in 2014. He received the Ph.D. degree in Electrical Engineering from University of Strathclyde, Glasgow, U.K., in 2020. He is currently a associate researcher with University of Strathclyde in Glasgow, UK. His research interests include modelling of power electronic converters, grid integration of renewable power, and stability analysis of the HVDC transmission systems.